



## Spectral energy transfers and kinetic-potential energy exchange in rotating stratified turbulence

Tianyi Li,<sup>1,2</sup> Minping Wan <sup>1,3,\*</sup>, Jianchun Wang <sup>1,3</sup> and Shiyi Chen<sup>1,2,3,†</sup>

<sup>1</sup>Guangdong Provincial Key Laboratory of Turbulence Research and Applications, Department of Mechanics and Aerospace Engineering, Southern University of Science and Technology, Shenzhen, Guangdong 518055, People's Republic of China

<sup>2</sup>State Key Laboratory of Turbulence and Complex Systems, College of Engineering, Peking University, Beijing 100871, People's Republic of China

<sup>3</sup>Southern Marine Science and Engineering Guangdong Laboratory (Guangzhou), 1119 Haibin Road, Nansha District, Guangzhou 511458, China



(Received 9 May 2020; accepted 1 December 2020; published 31 December 2020)

Direct numerical simulations of forced homogeneous rotating stratified turbulence are carried out with the same Rossby number and different Froude numbers. We investigated the effects of different stratification on energy transfers across scales and kinetic-potential energy exchange in Fourier space in the inverse energy cascade range. When the stratification is weak, almost all the kinetic energy flux in the inertial range comes from two-dimensional and three-dimensional (2D-3D) coupling interactions and 2D dynamics dominates at very large scales, which are similar to those in the purely rotating case. However, compared with the purely rotating case, the inverse cascade is weakened through the kinetic-potential energy exchange induced by 3D wave-vortical interactions. The total kinetic-potential energy exchange is found to oscillate at later times, which is produced by 2D inertia-gravity waves with fixed wave numbers. When the stratification is strong, the distributions of decomposed kinetic fluxes are different from those in purely rotating case. The magnitude of 2D-3D coupling energy flux becomes small and 3D-mode energy flux is important near the forcing scales. Besides, homo- and heterochiral energy fluxes are different in the inverse cascade. The kinetic-potential energy exchange under strong stratification mainly comes from 3D modes and wave-vortical interactions. Strengths of stratification negligibly affect properties of locality of the kinetic energy cascade, which is infrared local and ultraviolet nonlocal.

DOI: [10.1103/PhysRevFluids.5.124804](https://doi.org/10.1103/PhysRevFluids.5.124804)

### I. INTRODUCTION

Rotation and stratification play important roles in many geophysical and industrial turbulent flows [1–3]. In rotating stratified turbulence, both stable and oscillatory modes, the latter closely related to dispersive waves, are introduced to the relevant linear dynamics by Coriolis and buoyancy forces (see, e.g., Ref. [4]). There are two important dimensionless numbers, Rossby number  $Ro = U/fl$  and Froude number  $Fr = U/Nl$ , where  $U$  and  $l$  are the characteristic velocity and length respectively,  $f$  is the Coriolis parameter, and  $N$  is the Brunt-Väisälä frequency.  $Ro$  (or  $Fr$ ) signifies the ratio of inertial term to Coriolis force (or buoyancy force). As  $Ro$  (or  $Fr$ ) gets smaller, the strength of the rotation (or stratification) becomes stronger.

\*wanmp@sustech.edu.cn

†chensy@sustech.edu.cn

Extensive researches indicate that an inverse cascade of energy could be sustained in rapidly rotating turbulence [5,6], which leads to the formation of 2D large-scale vortical structures parallel to the rotation axis. Classical Taylor-Proudman theorem displays that strong rotation makes the flow quasi-two-dimensional (quasi-2D) [7,8]. However, it is not applicable to explain the quasi-two-dimensionalization observed in experiments [9–14] and numerical studies [15–19], where  $Ro$  is moderate or the secular nonlinear dynamics is considered. To get a better asymptotic solution, the resonant wave theory [20,21] should be taken into account. Chen *et al.* [16] verified the resonant wave theory with direct numerical simulations. They also revealed that as the rotation rate increases, the vertically averaged horizontal velocity field of 3D Navier-Stokes (NS) equations converges to the velocity field of 2D NS equations. Buzzicotti *et al.* [22] further investigated interactions between the quasi-2D turbulence and the 3D background. They found that increasingly dominant homochiral interactions, which couple the 3D bulk and the two-dimensional three-component (2D3C) plane, generated the inverse cascade near the forcing scale. It was also shown that the energy in the 2D3C plane is transferred to large scales due to interactions between 2D modes.

The system is more complex when stratification is taken into account. Inertial waves in the purely rotating system become inertia-gravity waves, the frequencies of which depend on the rotation and stratification. For purely stratified turbulence without rotation, Herring and Métais [23] showed the existence of a weak inverse cascade for two-dimensional forcing when Froude number is sufficiently small. Smith and Waleffe [24] reported the generation of vertically sheared horizontal winds after a long integration time in forced stratified turbulence with a Froude number smaller than some critical value. The present paper aims to address effects of different stratification on energy transfers in the inverse cascade range of rotating stratified turbulence. Marino *et al.* [25] found that in the range  $1/2 \leq N/f \leq 2$ , where the transfer of energy from 3D to 2D modes is most efficient, the inverse cascade of kinetic energy is faster than that in the purely rotating case. Oks *et al.* [26] then showed that in this range slow quasigeostrophic modes are dominant, while fast inertia-gravity waves are weaker in the flow dynamics. However, there is still a lack of a systematic study of interactions between modes from different decompositions under different stratification.

Our present work also investigate the spectral property of kinetic-potential energy exchange in rotating stratified turbulence. In a previous study, we investigated the connection of kinetic-potential energy exchange with flow structures in physical space [27]. It is important to note that kinetic-potential energy exchange does not produce any transfer across scales. It modifies the properties of the energy flux through acting as source or sink at different wave numbers. Inertia-gravity waves, ones of linear modes for rotating stratified turbulence [28–30], are closely relevant to kinetic-potential energy exchange. Therefore, investigating kinetic-potential energy exchange is important to understand the wave characteristics of the system, such as the breakdown of balance [31–33].

Another question of interest in rotating stratified turbulence is the locality of the energy cascade. For isotropic turbulence, Kolmogorov [34] assumed that the energy transfer across scales is local. The locality of cascades has been extensively investigated in hydrodynamic turbulence [35–37] and magnetohydrodynamic turbulence [38,39]. In rotating turbulence at intermediate Rossby number, Bourouiba, Straub, and Waite [40] showed that the dominant energy transfers to the large-scale 2D columnar vortices are nonlocal. However, the issue of locality has not been studied in rotating stratified turbulence, which is investigated in present work.

The remainder of this paper is arranged as follows. In Sec. II, we present the numerical setup of the simulations. We introduce the different decompositions for analysis of the energy flux in Sec. III. Section IV gives the simulation results, focusing on how different stratification impacts energy transfers across scales and the kinetic-potential energy exchange. Finally, we summarize our conclusions in Sec. V.

## II. NUMERICAL SETUP

Consider turbulent flows in the presence of vertical system rotation and stable stratification with gravity  $\mathbf{g}$  in the  $z$  direction, and the density is given by  $\rho = \rho_0 + \sigma z + \rho'(\mathbf{x}, t)$ , where  $\sigma$  indicates

TABLE I. Simulation parameters:  $n_p$ , number of collocation points per spatial direction;  $k_f$ , the forced wave number;  $\text{Re}_{(q)}$ , Reynolds number based on hyperviscosity;  $\text{Ro} = (\epsilon_f k_f^2)^{1/3}/(2\Omega)$ , Rossby number defined in terms of the energy injection properties;  $\text{Fr} = (\epsilon_f k_f^2)^{1/3}/N$ , Froude number ( $\text{Fr} = \infty$  indicates the purely rotating case) defined in terms of the energy injection properties;  $\text{Re}_{b,(q)} = \text{Re}_{(q)}\text{Fr}^2$ , buoyancy Reynolds number;  $l_b = U/N$ , the buoyancy length scale at  $480\tau_0$ , where  $U$  is the r.m.s. velocity;  $t_e$ , overall integration time;  $\tau_0 = l_0/u_0$ , the initial large-eddy turnover time.

Run	$n_p$	$k_f$	$\text{Re}_{(q)}$	Ro	Fr	$\text{Re}_{b,(q)}$	$l_b$	$t_e$
1	256	48	2100	0.033	$\infty$	$\infty$	$\infty$	$496\tau_0$
2	256	48	2100	0.033	0.42	368	0.14	$496\tau_0$
3	256	48	2100	0.033	0.052	6	0.011	$496\tau_0$

the mean stratification. We assume a mechanical forcing function  $\mathbf{f}$  that forces the flow. In the limit  $|\rho - \rho_0| \ll \rho_0$ , we obtain the Boussinesq equations in the rotating frame of reference:

$$\partial_t \mathbf{u} + \mathbf{u} \cdot \nabla \mathbf{u} + 2\Omega \mathbf{e}_z \times \mathbf{u} = -N \mathbf{e}_z \phi - \nabla P + \nu \Delta \mathbf{u} + \mathbf{f}, \quad (1)$$

$$\partial_t \phi + \mathbf{u} \cdot \nabla \phi = N \mathbf{e}_z \cdot \mathbf{u} + \kappa \Delta \phi, \quad (2)$$

$$\nabla \cdot \mathbf{u} = 0. \quad (3)$$

Here  $\Omega$  is the rotation rate,  $N = \sqrt{g\sigma/\rho_0}$  is the buoyancy (Brunt-Väisälä) frequency, and  $\phi(\mathbf{x}, t) = \sqrt{g/\sigma\rho_0}\rho'(\mathbf{x}, t)$  has the dimension of velocity.  $\nu$  is the kinematic viscosity and  $\kappa$  is the diffusivity. Rossby and Froude numbers are defined as

$$\text{Ro} = \frac{u_f}{2\Omega l_f}, \quad \text{Fr} = \frac{u_f}{N l_f}, \quad (4)$$

where  $u_f = (\epsilon_f l_f)^{1/3}$  is the rms velocity at the forcing scale  $l_f$  and  $\epsilon_f$  is the kinetic energy input rate.

The velocity field is initialized with homogeneous isotropic turbulence and  $\phi(\mathbf{x}, 0) = 0$ . By a parallelized pseudospectral code, Eqs. (1)–(3) have been integrated for the transient flow state. Note that all the conclusions are robust according to the results from different initial conditions and forcing scales. We adopted an intermediate forcing wave number  $k_f$  and focused on the inverse-cascade range  $k < k_f$ . To extend the inertial range, the normal viscous term  $\nu \Delta \mathbf{u}$  has been replaced with the hyperviscous term  $(-1)^{q+1} \nu_q (\nabla)^{2q} \mathbf{u}$  where  $q = 8$  and Reynolds number based on hyperviscosity is defined as  $\text{Re}_{(q)} = \epsilon^{1/3}/(\nu_q k_f^{2(q-1/3)})$ . Similarly, the hyperdiffusive term  $(-1)^{q+1} \kappa_q (\nabla)^{2q} \phi$  is adopted to replace the normal diffusive term  $\kappa \Delta \phi$ . For more details of the numerical setup, please refer to our previous paper [27].

Simulation parameters are shown in Table I. To study the effects of stratification, we conducted three simulation cases with the same Rossby number  $\text{Ro} = 0.033$ , but with different Froude numbers  $\text{Fr} = \infty$  (for the purely rotating case),  $\text{Fr} = 0.42$ , and  $\text{Fr} = 0.052$ . We adopted sufficiently long integration time, since it is necessary for the generation of slow large scales [24]. Therefore, a moderate resolution with  $256^3$  grid was used and a grid independence study showed that our results do not change with further grid refinement.

### III. ANALYTICAL METHODS

In this section, we give a brief introduction of analytical methods adopted in our simulations, including 2D-3D decomposition, helical decomposition, and linear-eigenmode decomposition. They have been widely used in analyzing the energy transfer in rotating and rotating stratified turbulence [22,24,29,41,42].

### A. 2D-3D decomposition

Marino *et al.* [25] showed that the efficiency of the energy transfer from 3D to 2D modes is closely relevant to inverse cascades in rotating stratified turbulence. To numerically assess the energy transfer inside the 2D/3D modes and mutual interactions between 2D and 3D modes, we use the 2D-3D decomposition, which divides the total wave-number space into two subsets [43]

$$\begin{aligned} V &= \{\mathbf{k} \mid k_x, k_y \text{ and } k_z = 0\}, \\ W &= \{\mathbf{k} \mid k_x, k_y \text{ and } k_z \neq 0\}. \end{aligned} \quad (5)$$

The 2D-3D decomposition is the slow-fast decomposition for purely rotating turbulence [22]. Any scalar or vector field can be separated into the 2D and 3D components by applying this decomposition. Take velocity field  $\hat{\mathbf{u}}(\mathbf{k})$  as an example, we have

$$\hat{\mathbf{u}}(\mathbf{k}) = \begin{cases} \hat{\mathbf{u}}_{2D}(\mathbf{k}) & \text{if } \mathbf{k} = \mathbf{k}_{2D} \in V, \\ \hat{\mathbf{u}}_{3D}(\mathbf{k}) & \text{if } \mathbf{k} = \mathbf{k}_{3D} \in W. \end{cases} \quad (6)$$

Projecting the momentum equation on the two submanifolds  $V$  and  $W$  derives evolution equations of  $\mathbf{u}_{2D}$  and  $\mathbf{u}_{3D}$  including nonlinear interactions between 2D and 3D modes:

$$\partial_t \mathbf{u}_{2D} + \mathbf{u}_{2D} \cdot \nabla \mathbf{u}_{2D} = -P_{2D}(\mathbf{u}_{3D} \cdot \nabla \mathbf{u}_{3D}) - N\mathbf{e}_z \phi_{2D} - P_{2D}(\nabla P) + \nu \Delta \mathbf{u}_{2D} + \mathbf{f}_{2D}, \quad (7)$$

$$\begin{aligned} \partial_t \mathbf{u}_{3D} + P_{3D}(\mathbf{u}_{3D} \cdot \nabla \mathbf{u}_{3D}) &= -\mathbf{u}_{2D} \cdot \nabla \mathbf{u}_{3D} - \mathbf{u}_{3D} \cdot \nabla \mathbf{u}_{2D} \\ &\quad - N\mathbf{e}_z \phi_{3D} - P_{3D}(\nabla P) + \nu \Delta \mathbf{u}_{3D} + \mathbf{f}_{3D}. \end{aligned} \quad (8)$$

Here,  $P_{2D}$  and  $P_{3D}$  are the projectors on the wave-number subsets  $V$  and  $W$ , respectively. Equations of kinetic energy in 2D and 3D modes can be written by multiplying Eq. (7) by  $\mathbf{u}_{2D}$  and Eq. (8) by  $\mathbf{u}_{3D}$ :

$$\begin{aligned} \partial_t \frac{1}{2} \mathbf{u}_{2D}^2 + \mathbf{u}_{2D} \cdot (\mathbf{u}_{2D} \cdot \nabla \mathbf{u}_{2D}) &= -\mathbf{u}_{2D} \cdot (P_{2D}[\mathbf{u}_{3D} \cdot \nabla \mathbf{u}_{3D}]) \\ &\quad - N(\mathbf{u}_{2D} \cdot \mathbf{e}_z) \phi_{2D} - \mathbf{u}_{2D} \cdot P_{2D}(\nabla P) + \nu \mathbf{u}_{2D} \cdot \Delta \mathbf{u}_{2D} + \mathbf{u}_{2D} \cdot \mathbf{f}_{2D}, \end{aligned} \quad (9)$$

$$\begin{aligned} \partial_t \frac{1}{2} \mathbf{u}_{3D}^2 + \mathbf{u}_{3D} \cdot (P_{3D}[\mathbf{u}_{3D} \cdot \nabla \mathbf{u}_{3D}]) &= -\mathbf{u}_{3D} \cdot (\mathbf{u}_{2D} \cdot \nabla \mathbf{u}_{3D}) - \mathbf{u}_{3D} \cdot (\mathbf{u}_{3D} \cdot \nabla \mathbf{u}_{2D}) \\ &\quad - N(\mathbf{u}_{3D} \cdot \mathbf{e}_z) \phi_{3D} - \mathbf{u}_{3D} \cdot P_{3D}(\nabla P) + \nu (\mathbf{u}_{3D} \cdot \Delta \mathbf{u}_{3D}) \\ &\quad + \mathbf{u}_{3D} \cdot \mathbf{f}_{3D}. \end{aligned} \quad (10)$$

We Fourier transform Eqs. (9) and (10), and obtain the equation of kinetic energy in Fourier space:

$$\sum_{k'=1}^k \partial_t E(k', t) = \Pi_K(k, t) - \Pi_{KP}(k, t) + D(k, t) + F(k, t), \quad (11)$$

where  $\Pi_K$  is the kinetic energy flux, and  $\Pi_{KP}$  is the conversion rate of kinetic energy to potential energy.  $D$  and  $F$  are the dissipation and the energy input rate in the Fourier-space sphere with a radius  $k$ , respectively.

$\Pi_K$  comes from three different contributions:

$$\Pi_K(k) = \Pi_{2D \rightleftharpoons 2D}(k) + \Pi_{3D \rightleftharpoons 3D}(k) + \Pi_{3D \rightleftharpoons 2D}(k), \quad (12)$$

where

$$\Pi_{2D \rightleftharpoons 2D}(k) = - \sum_{\substack{k \in V \\ |k| \leq k}} ik_j \hat{u}_i^*(\mathbf{k}) \sum_{\mathbf{p}, \mathbf{q} \in V} \hat{u}_i(\mathbf{p}) \hat{u}_j(\mathbf{q}) \delta(\mathbf{p} + \mathbf{q} - \mathbf{k}) \quad (13)$$

and

$$\Pi_{3D \rightleftharpoons 3D}(k) = - \sum_{\substack{k \in W \\ |k| \leq k}} ik_j \hat{u}_i^*(\mathbf{k}) \sum_{\mathbf{p}, \mathbf{q} \in W} \hat{u}_i(\mathbf{p}) \hat{u}_j(\mathbf{q}) \delta(\mathbf{p} + \mathbf{q} - \mathbf{k}) \quad (14)$$

are energy fluxes transferring energy only among the 2D and the 3D modes, respectively.  $\Pi_{3D \rightleftharpoons 2D}$  represents the energy flux through the 2D-3D coupling interactions:

$$\Pi_{3D \rightleftharpoons 2D}(k) = \Pi_{3D \rightleftharpoons 2D}^a(k) + \Pi_{3D \rightleftharpoons 2D}^b(k) + \Pi_{3D \rightleftharpoons 2D}^c(k), \quad (15)$$

where

$$\Pi_{3D \rightleftharpoons 2D}^a(k) = - \sum_{\substack{k \in W \\ |k| \leq k}} ik_j \hat{u}_i^*(\mathbf{k}) \sum_{\substack{\mathbf{p} \in V \\ \mathbf{q} \in W}} \hat{u}_i(\mathbf{p}) \hat{u}_j(\mathbf{q}) \delta(\mathbf{p} + \mathbf{q} - \mathbf{k}), \quad (16)$$

$$\Pi_{3D \rightleftharpoons 2D}^b(k) = - \sum_{\substack{k \in V \\ |k| \leq k}} ik_j \hat{u}_i^*(\mathbf{k}) \sum_{\substack{\mathbf{p} \in W \\ \mathbf{q} \in W}} \hat{u}_i(\mathbf{p}) \hat{u}_j(\mathbf{q}) \delta(\mathbf{p} + \mathbf{q} - \mathbf{k}), \quad (17)$$

and

$$\Pi_{3D \rightleftharpoons 2D}^c(k) = - \sum_{\substack{k \in W \\ |k| \leq k}} ik_j \hat{u}_i^*(\mathbf{k}) \sum_{\substack{\mathbf{p} \in W \\ \mathbf{q} \in V}} \hat{u}_i(\mathbf{p}) \hat{u}_j(\mathbf{q}) \delta(\mathbf{p} + \mathbf{q} - \mathbf{k}). \quad (18)$$

Both  $\Pi_{3D \rightleftharpoons 2D}^a$  and  $\Pi_{3D \rightleftharpoons 2D}^c$  come from Eq. (10), and  $\Pi_{3D \rightleftharpoons 2D}^b$  comes from Eq. (9). They quantify contributions from different classes of triadic interactions.

$\Pi_{KP}$  produces no transfer across scales, being composed of the 2D and the 3D contributions:

$$\Pi_{KP}(k) = \Pi_{KP,2D}(k) + \Pi_{KP,3D}(k), \quad (19)$$

where

$$\Pi_{KP,2D}(k) = \sum_{\substack{k \in V \\ |k| \leq k}} \text{Re}[N \hat{u}_z^*(\mathbf{k}) \hat{\phi}(\mathbf{k})], \quad (20)$$

and

$$\Pi_{KP,3D}(k) = \sum_{\substack{k \in W \\ |k| \leq k}} \text{Re}[N \hat{u}_z^*(\mathbf{k}) \hat{\phi}(\mathbf{k})]. \quad (21)$$

## B. Helical decomposition

The well-known helical decomposition [44,45] projects the Fourier components of the divergence-free velocity field onto the two eigenvectors of the curl operator:

$$\hat{\mathbf{u}}_k(t) = \hat{\mathbf{u}}_k^+(t) + \hat{\mathbf{u}}_k^-(t) = \hat{\mathbf{u}}_k^+(t) \mathbf{h}^+(\mathbf{k}) + \hat{\mathbf{u}}_k^-(t) \mathbf{h}^-(\mathbf{k}), \quad (22)$$

where  $\mathbf{h}^\pm$  satisfies  $i\mathbf{k} \times \mathbf{h}^\pm = \pm k \mathbf{h}^\pm$  and has a sign-definite helicity.

Recent researches [41,42] have shown that homochiral triadic interactions lead to a reverse energy transfer from small to large scales in homogeneous isotropic turbulence. Moreover, homochiral and heterochiral triadic interactions have also been investigated in purely rotating turbulence [22]. The homochiral energy flux is

$$\Pi^{\text{HO}}(k) = - \sum_{|k| \leq k} \sum_{s \in \{+, -\}} \hat{\mathbf{u}}_k^{s*} \sum_{\mathbf{q} = \mathbf{k} - \mathbf{p}} (i\mathbf{k} \cdot \hat{\mathbf{u}}_p^s) \hat{\mathbf{u}}_q^s, \quad (23)$$

and the heterochiral energy flux is

$$\Pi^{\text{HE}}(k) = \Pi_K(k) - \Pi^{\text{HO}}(k). \quad (24)$$

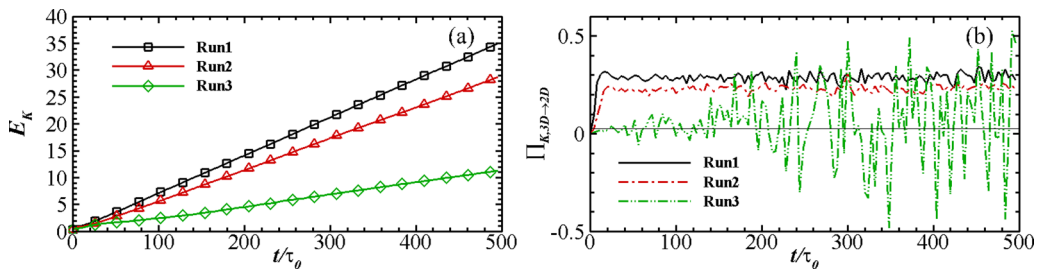


FIG. 1. (a) Kinetic energy  $E_K$  and (b) kinetic energy flux from 3D modes to 2D modes  $\Pi_{K,3D \rightarrow 2D}$  as functions of time for all simulations. The solid horizontal line in panel (b) indicates  $\Pi_{K,3D \rightarrow 2D} = 0$  for reference.

### C. Linear-eigenmode decomposition

Three eigenmodes of the linearized Eqs. (1)–(3) when  $\nu = \kappa = f = 0$  have the form of  $\mathbf{Z}^s(\mathbf{k})e^{i\sigma^s(\mathbf{k})t}$ , where  $s \in \{+, -, 0\}$ .  $\mathbf{Z}^+$  and  $\mathbf{Z}^-$  are wave modes with

$$\sigma^\pm(\mathbf{k}) = \pm \sqrt{f^2 \frac{k_z^2}{k^2} + N^2 \frac{k_h^2}{k^2}}, \quad (25)$$

where  $k_h = \sqrt{k_x^2 + k_y^2}$ .  $\mathbf{Z}^0$  is the vortical mode and has a zero frequency. We can normalize the modes and expand the Fourier-transformed velocity and buoyancy as

$$\begin{pmatrix} \hat{\mathbf{u}}_{\mathbf{k}} \\ \hat{\phi}_{\mathbf{k}} \end{pmatrix}(t) = a_{\mathbf{k}}^+(t)\mathbf{Z}^+(\mathbf{k}) + a_{\mathbf{k}}^-(t)\mathbf{Z}^-(\mathbf{k}) + a_{\mathbf{k}}^0(t)\mathbf{Z}^0(\mathbf{k}). \quad (26)$$

For the purely rotating case where  $N = 0$ ,  $\mathbf{Z}^0$  is trivial, while  $\mathbf{Z}^+$  and  $\mathbf{Z}^-$  are also called inertial waves which have the same form as helical waves. More detailed description of the linear modes can be found in Refs. [24,29,30].

## IV. RESULTS

### A. Kinetic energy, potential energy, and their conversion rate

Figure 1(a) shows the time evolution of the kinetic energy  $E_K$  for all three simulations, where the time is normalized by the initial large-eddy turnover time  $\tau_0$ . For the three values of Fr considered, a stable growth of  $E_K$  is obtained after  $t = 40\tau_0$ , and the growth rate decreases as Fr decreases. To understand the effect of different stratification on the growth of  $E_K$ , we consider the flux of kinetic energy from 3D modes to 2D modes [25]

$$\Pi_{K,3D \rightarrow 2D} = \Pi_{3D \rightleftharpoons 2D}^b(\infty). \quad (27)$$

A positive  $\Pi_{K,3D \rightarrow 2D}$  indicates the amount of kinetic energy transferred from 3D modes to 2D modes and a negative  $\Pi_{K,3D \rightarrow 2D}$  represents a reverse transfer direction. The time evolution of  $\Pi_{K,3D \rightarrow 2D}$  for all cases is plotted in Fig. 1(b). For Run1 and Run2,  $\Pi_{K,3D \rightarrow 2D}$  reaches a stationary state after  $t = 20\tau_0$ , with a little larger value in Run1, where the kinetic energy grows fastest. However,  $\Pi_{K,3D \rightarrow 2D}$  fluctuates dramatically around a value close to zero for Run3.

Figures 2(a) and 2(b) display potential energy  $E_P$  and the conversion rate of kinetic energy to potential energy  $E_{KP} = \Pi_{KP}(\infty)$  for Run2 and Run3. For both cases,  $E_P$  reaches a stationary state, which is different from the behavior of  $E_K$ . For Run2, we observe that  $E_{KP}$  begins to oscillate when  $t \approx 200\tau_0$  with an increasing magnitude and a period of  $37\tau_0$ . The magnitude does not increase infinitely when we continue the integration. However, in Run3  $E_{KP}$  fluctuates violently around a positive value, indicating a continuous conversion from kinetic energy to potential energy.

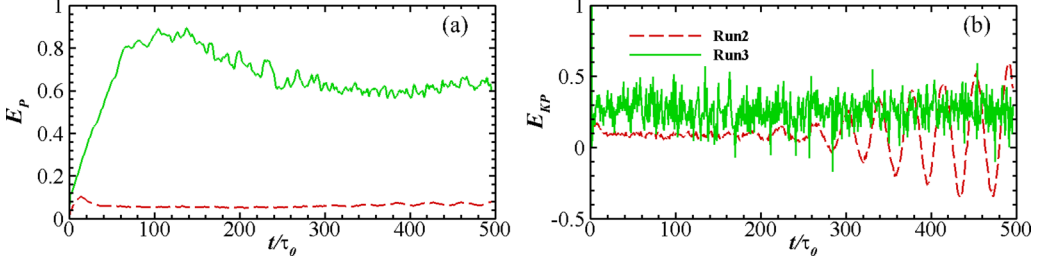


FIG. 2. (a) Potential energy  $E_p$  and (b) the conversion rate of kinetic energy to potential energy  $E_{KP}$  as functions of time for Run2 and Run3.

To further understand  $\Pi_{K,3D \rightarrow 2D}$  and  $E_{KP}$  in Run2 and Run3, we calculate the fluxes from kinetic energy to potential energy through 3D modes and 2D modes,  $\Pi_{KP,3D \rightarrow 3D} = \Pi_{KP,3D}(\infty)$  and  $\Pi_{KP,2D \rightarrow 2D} = \Pi_{KP,2D}(\infty)$ , respectively. When positive,  $\Pi_{KP,3D \rightarrow 3D}$  (or  $\Pi_{KP,2D \rightarrow 2D}$ ) gives the amount of kinetic energy transferred to potential energy through 3D modes (or 2D modes) per unit of time, and represents a reverse transfer when it is negative. As shown in Fig. 3 (left), for Run2,  $\Pi_{KP,3D \rightarrow 3D}$  reaches a stationary state after  $t = 20\tau_0$ , holding a small positive value. This means that there is a small amount of kinetic energy transferring to potential energy continuously through 3D modes.  $\Pi_{KP,2D \rightarrow 2D}$  is close to zero at early times and oscillates around zero with an increasing magnitude after  $t \approx 200\tau_0$ . Therefore,  $\Pi_{KP,3D \rightarrow 3D}$  and  $\Pi_{KP,2D \rightarrow 2D}$  are responsible for the mean value and the oscillation of  $\Pi_{KP}$ , respectively. Figure 3 (left) also shows that  $\Pi_{K,3D \rightarrow 2D} + \Pi_{KP,3D \rightarrow 3D}$  in Run2 is close to  $\Pi_{K,3D \rightarrow 2D}$  in Run1. This indicates that compared with Run1 (the purely rotating case), the weak stratification in Run2 does not change the time behavior of  $\Pi_{K,3D \rightarrow 2D}$  but weakens  $\Pi_{K,3D \rightarrow 2D}$  by transferring a small amount of kinetic energy to potential energy in 3D modes. For Run3,  $\Pi_{KP,2D \rightarrow 2D}$  is close to zero at all times and  $\Pi_{KP,3D \rightarrow 3D}$  fluctuates around a value comparable with  $\Pi_{K,3D \rightarrow 2D}$  in Run1, as displayed in Fig. 3 (right). Note that although  $\Pi_{K,3D \rightarrow 2D} + \Pi_{KP,3D \rightarrow 3D}$  in Run3 fluctuates around the value of  $\Pi_{K,3D \rightarrow 2D}$  in Run1, the time behavior of  $\Pi_{K,3D \rightarrow 2D}$  in Run3 is totally different from that in Run1. The strong stratification significantly modifies the flow at this point. More detailed analysis will be displayed in Sec. IV C.

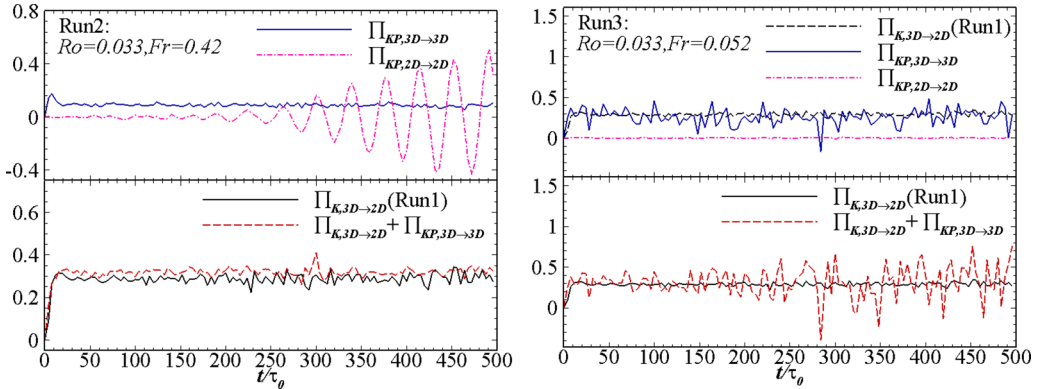


FIG. 3. Time evolutions of different energy fluxes for Run2 (left) and Run3 (right): the kinetic flux from 3D modes to 2D modes,  $\Pi_{K,3D \rightarrow 2D}$ ; the flux from kinetic energy to potential energy in 3D modes and in 2D modes,  $\Pi_{KP,3D \rightarrow 3D}$  and  $\Pi_{KP,2D \rightarrow 2D}$ . Note that  $\Pi_{K,3D \rightarrow 2D}$  for Run1 is shown for reference.



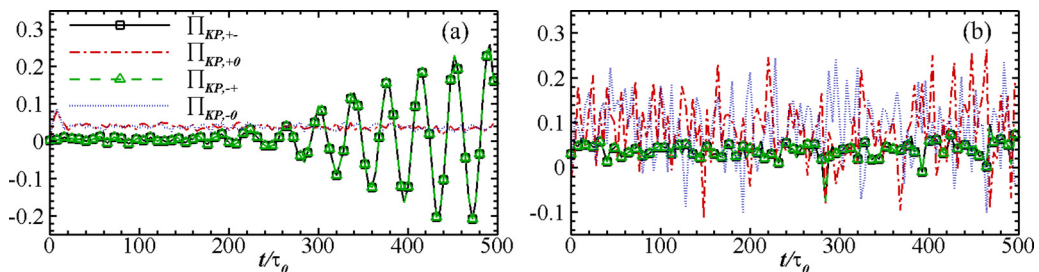


FIG. 4. Fluxes from kinetic energy to potential energy by interactions among different linear eigenmodes obtained from (a) Run2 and (b) Run3.

To understand the evolution of kinetic-potential energy exchange  $E_{KP}$ , here we consider the contribution to  $E_{KP}$  from the interaction among different linear eigenmodes

$$\Pi_{KP,s_1s_2} = \langle Nu_z^{s_1} \phi^{s_2} \rangle, \quad (28)$$

where  $s_1, s_2 \in \{+, -, 0\}$  (see Sec. III C).  $\Pi_{KP,s_1s_2}$  represents the conversion of kinetic energy to potential energy by the interaction of the  $s_1$  eigenmode with the  $s_2$  eigenmode. Note that  $\Pi_{KP,+} = \Pi_{KP,-}$  and  $\Pi_{KP,0s_2} = 0$  because  $u_z^0(x) = 0$ . For Run2 and Run3, we found that  $\Pi_{KP,++}$  and  $\Pi_{KP,--}$  are negligible and plotted  $\Pi_{KP,+}$ ,  $\Pi_{KP,+0}$ ,  $\Pi_{KP,-}$  and  $\Pi_{KP,-0}$  in Fig. 4. Figure 4(a) shows that for Run2  $\Pi_{KP,+0}$  and  $\Pi_{KP,-0}$  have nearly equal positive values, and  $\Pi_{KP,+}$  ( $\Pi_{KP,-}$ ) with a zero mean value is responsible for the oscillation of  $E_{KP}$ . This indicates that the mean conversion of kinetic energy to potential energy is realized through the wave-vortical interactions and the oscillation is attributed to the interactions between different inertia-gravity waves. For Run3, the interactions between different inertia-gravity waves give small contributions to  $E_{KP}$  and the wave-vortical interactions lead to the main part of  $E_{KP}$  [Fig. 4(b)].

## B. Energy spectra

Figure 5 shows the evolution of 3D kinetic energy spectra for all the simulations. Kinetic energy is transferred to the large scales after the addition of rotation and stratification [Figs. 5(a), 5(c), and 5(e)], which is consistent with previous studies [16,24]. The large-scale kinetic energy grows faster for Run1 and Run2 than for Run3. Figures 5(b), 5(d), and 5(f) show the spectra of kinetic energy  $E_K(k)$ , 2D-mode kinetic energy  $E_K(k_h, k_z = 0)$  and kinetic energy from vertically averaged horizontal velocity  $E_{k,xy}(k_h, k_z = 0)$  at  $t = 480\tau_0$ .  $E_K(k_h, k_z = 0)$  and  $E_{k,xy}(k_h, k_z = 0)$  are, respectively, defined as

$$E_K(k_h, k_z = 0) = \sum_{\substack{k_z=0 \\ k \leq k_h < k+1}} \frac{1}{2} |\hat{\mathbf{u}}(\mathbf{k})|^2 \quad (29)$$

and

$$E_{K,xy}(k_h, k_z = 0) = \sum_{\substack{k_z=0 \\ k \leq k_h < k+1}} \frac{1}{2} [|\hat{u}_x(\mathbf{k})|^2 + |\hat{u}_y(\mathbf{k})|^2]. \quad (30)$$

These three spectra all collapse together at large scales, indicating the two-dimensionalization of the flow. For Run3, the wave-number range where the three types of spectra collapse together is narrower than that for Run1 and Run2. Therefore, the degree of the two-dimensionalization of velocity field decreases when strong stratification exists.

Figure 6 plots the evolution of 3D potential energy spectra for Run2 and Run3. Figures 6(a) and 6(c) show that the variation of the potential energy concentrates on large scales. Figures 6(b) and



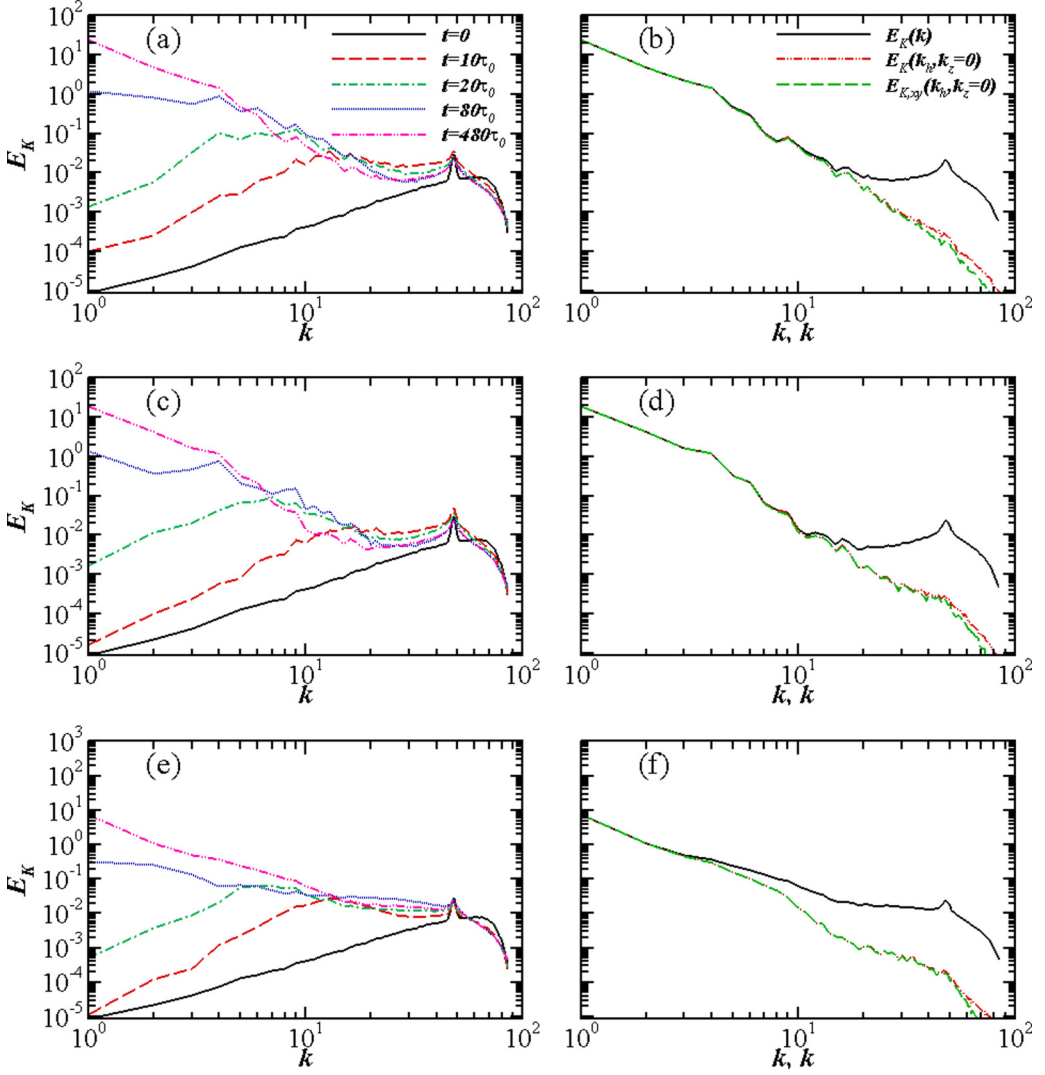


FIG. 5. (a), (c), (e) The time evolution of the kinetic energy spectrum for (a) Run1, (c) Run2, and (e) Run3 at different times. (b), (d), (f) Three types of kinetic energy spectra from one realization at time  $t = 480\tau_0$  for (b) Run1, (d) Run2, and (f) Run3.

**6(d)** show the spectra of potential energy  $E_P(k)$  and 2D potential energy  $E_P(k_h, k_z = 0)$  at  $t = 480\tau_0$ , where  $E_P(k_h, k_z = 0)$  is defined as

$$E_P(k_h, k_z = 0) = \sum_{\substack{k_z=0 \\ k < k_h < k+1}} \frac{1}{2} |\hat{\phi}(\mathbf{k})|^2. \quad (31)$$

These two spectra are widely different at all scales for Run2 and Run3, indicating that the potential energy widely distributes in 3D modes.

We further study the spectra of the conversion rate of kinetic energy to potential energy

$$E_{KP}(k) = \sum_{k \leq |\mathbf{k}| < k+1} \text{Re}[N\hat{u}_z^*(\mathbf{k})\hat{\phi}(\mathbf{k})]. \quad (32)$$

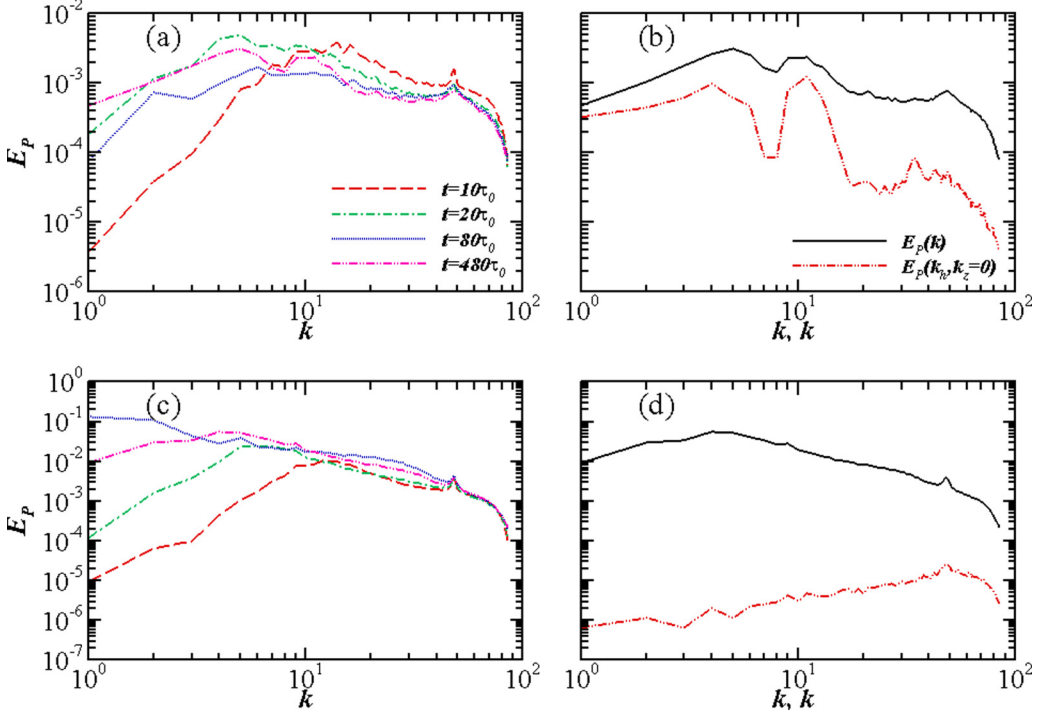


FIG. 6. (a), (c) The time evolution of the potential energy spectrum for (a) Run2 and (c) Run3 at different times. (b), (d) Two types of potential energy spectra from one realization at time  $t = 480\tau_0$  for (b) Run2 and (d) Run3.

As shown in Fig. 7, for Run2, the magnitude of the spectra is small for all wave numbers at early times. When  $t \gtrsim 200\tau_0$ , the fluctuation of  $E_{KP}(k)$  with a large magnitude concentrates on  $5 \lesssim k \lesssim 10$  [Fig. 7(a)]. For Run3, Fig. 7(c) shows that  $E_{KP}(k)$  fluctuates at almost all scales. Figures 7(b) and 7(d) show the 3D and 2D spectra of the conversion rate of kinetic energy to potential energy,  $E_{KP}(k)$  and  $E_{KP}(k_h, k_z = 0)$ , at  $t = 480\tau_0$ . Here,  $E_{KP}(k_h, k_z = 0)$  is defined as

$$E_{KP}(k_h, k_z = 0) = \sum_{\substack{k_z=0 \\ k \leq k_h < k+1}} \text{Re}[N\hat{u}_z^*(\mathbf{k})\hat{\phi}(\mathbf{k})]. \quad (33)$$

The collapse of these two spectra for Run2 indicates that nearly all kinetic-potential energy exchange comes from certain 2D modes after  $t \approx 200\tau_0$ . Those 2D modes are relevant to coherent flow structures [27]. For Run3,  $E_{KP}(k_h, k_z = 0)$  is negligible compared with  $E_{KP}(k)$ , indicating that the kinetic-potential energy exchange is totally 3D. To further investigate the difference between  $E_{KP}(k)$  in Run2 and that in Run3, we consider the vortical-mode energy spectrum and the wave-mode energy spectrum

$$E_V(k) = \sum_{k \leq |\mathbf{k}| < k+1} \frac{1}{2} a_{\mathbf{k}}^{0,*} a_{\mathbf{k}}^0 \quad (34)$$

and

$$E_W(k) = \sum_{k \leq |\mathbf{k}| < k+1} \frac{1}{2} (a_{\mathbf{k}}^{+,*} a_{\mathbf{k}}^+ + a_{\mathbf{k}}^{-,*} a_{\mathbf{k}}^-), \quad (35)$$

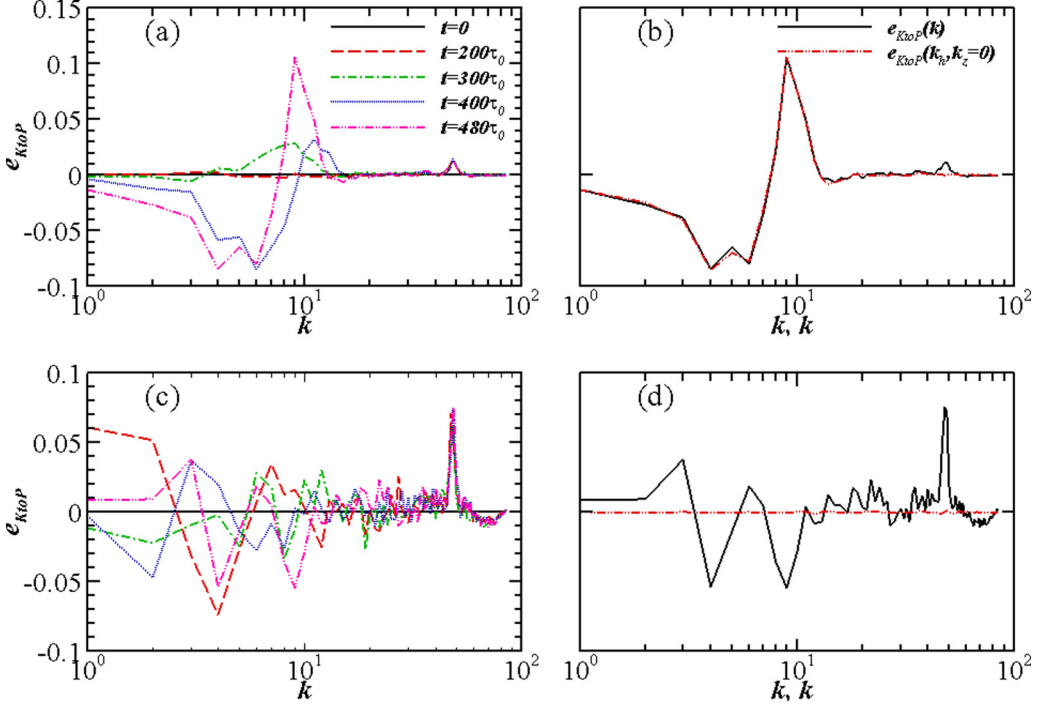


FIG. 7. (a), (c) The time evolution of the spectrum of the conversion rate of kinetic energy to potential energy for (a) Run2 and (c) Run3 at different times. (b), (d) Two types of spectra of the conversion rate from one realization at time  $t = 480\tau_0$  for (b) Run2 and (d) Run3.

as shown in Fig. 8. Figures 8(a) and 8(b) display that in Run2 and Run3  $E_V$  evolves similarly with time and is responsible for almost all the inverse cascade. However,  $E_W$  has an obvious bump at  $k \approx 10$  when  $t = 480\tau_0$  in Run2. The bump does not exist at early times in Run2 and at all times in Run3 [Figs. 8(c) and 8(d)]. The bump probably corresponds to the concentration of  $E_{KP}(k)$  at later times. Therefore, the oscillation of kinetic-potential energy exchange in Run2 is due to 2D wave modes with  $k \approx 10$ .

### C. Energy fluxes and transfer

Kinetic and potential energy fluxes are given by

$$\Pi_K(k, t) = - \sum_{|k| \leq k} \hat{u}^*(\mathbf{k}) \cdot \widehat{\mathbf{u} \times \boldsymbol{\omega}}(\mathbf{k}) \quad (36)$$

and

$$\Pi_P(k, t) = - \sum_{|k| \leq k} \hat{\phi}^*(\mathbf{k}) \cdot \widehat{\mathbf{u} \cdot \nabla \phi}(\mathbf{k}). \quad (37)$$

In Figs. 9 and 10, we show the evolution of kinetic and potential energy fluxes. For Run1 and Run2, the kinetic energy flux is nearly constant where  $20 < k < 40$  [Figs. 9(a) and 9(b)], indicating that there exists a conservative inverse cascade in kinetic energy. However, in Run3 the kinetic energy flux increases slowly with  $k$  where  $10 < k < 40$  and its magnitude in the inertial range is smaller than those in Run1 and Run2. Figure 10 displays that the potential energy flux changes negligibly at different times, and its shapes are similar in Run2 and Run3. There does not exist any conservative

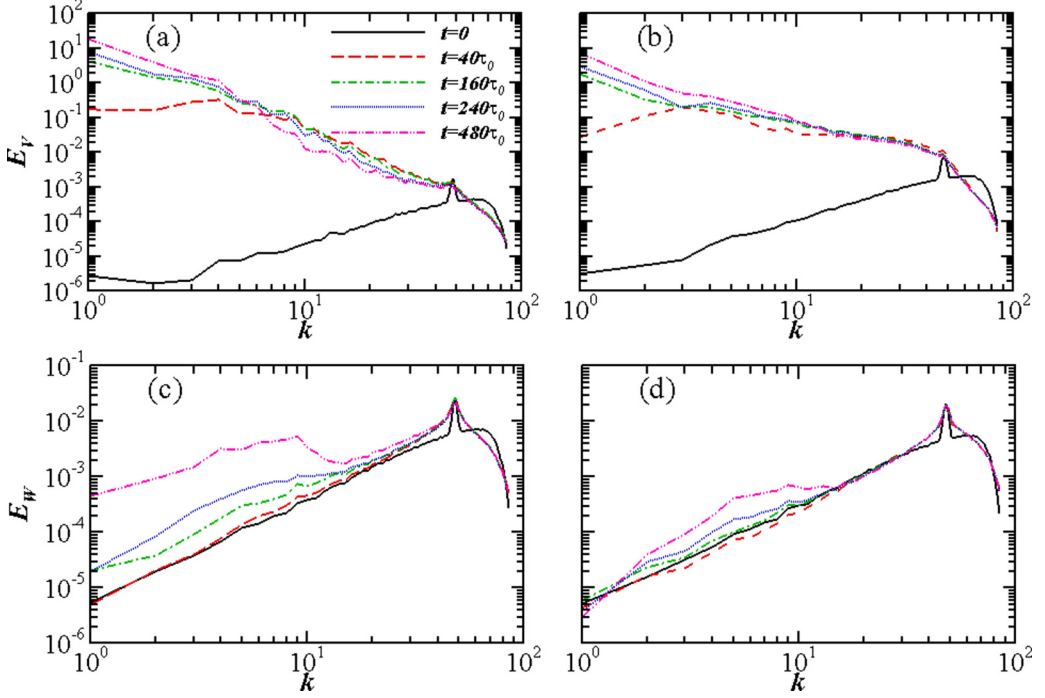


FIG. 8. The time evolution of (a), (b) the vortical-mode energy spectrum and (c), (d) the wave-mode energy spectrum for (a), (c) Run2 and (b), (d) Run3 at different times.

cascade in potential energy. Potential energy flux is positive at almost all wave numbers, which indicates that potential energy is transferred from large scales to small scales.

To investigate the effect of different stratification on the kinetic energy flux in detail, we analyze the different contributions based on the 2D-3D decomposition and the helical decomposition. Figs. 11(a), 11(c), and 11(e) present the kinetic energy flux with decomposed energy fluxes obtained from the 2D-3D decomposition, namely energy fluxes only among the 2D and the 3D modes [Eqs. (13) and (14)] and the energy flux from the 2D-3D coupling interactions Eq. (15); Figs. 11(b), 11(d), and 11(f) show  $\Pi_{3D\rightleftharpoons 2D}(k)$  with its three different contributions Eqs. (16)–(18). All the results come from one realization at  $t = 480\tau_0$ . For Run1 and Run2, in the inertial range almost all the negative  $\Pi_K(k)$  is due to  $\Pi_{3D\rightleftharpoons 2D}^b(k)$ , which comes from Eq. (10), the equation of kinetic energy in 2D modes. Only at very small wave numbers, 2D interactions dominate the dynamics with large negative values of  $\Pi_{2D\rightleftharpoons 2D}(k)$  [Figs. 11(a)–11(d)]. For Run3, Fig. 11(e) shows that 2D-3D coupling energy flux has small negative values where  $10 < k < k_f$ , and the energy flux among 3D modes is more important in the range  $k \lesssim k_f$ . The large-scale dynamics is dominated by 2D energy flux  $\Pi_{2D\rightleftharpoons 2D}(k)$  and 2D-3D coupling energy flux  $\Pi_{3D\rightleftharpoons 2D}(k)$ . The three contributions of  $\Pi_{3D\rightleftharpoons 2D}(k)$  are quite different from those in Run1 and Run2. As shown in Fig. 11(f),  $\Pi_{3D\rightleftharpoons 2D}^b(k)$  has a negative value where  $k > 10$  and  $\Pi_{3D\rightleftharpoons 2D}^a(k)$  has positive values where  $10 < k < k_f$ . They cancel each other, resulting small values of  $\Pi_{3D\rightleftharpoons 2D}(k)$ .

For all the cases at  $t = 480\tau_0$ , Fig. 12 compares the total kinetic energy flux  $\Pi_K(k)$  with homo- and heterochiral energy fluxes,  $\Pi^{\text{HO}}(k)$  and  $\Pi^{\text{HE}}(k)$ . For Run1 and Run2, homo- and heterochiral energy fluxes are nearly equal at  $k < k_f$ , both of which contribute to the inverse energy transfer. For Run3, the two fluxes are not constant in the inverse transfer range and do not equal at different scales. The analysis above shows that in rotating turbulence with weak stratification, only the inverse cascade is weakened and the distributions of different decomposed kinetic fluxes do not change, compared with the purely rotating case. However, the distributions of different decomposed

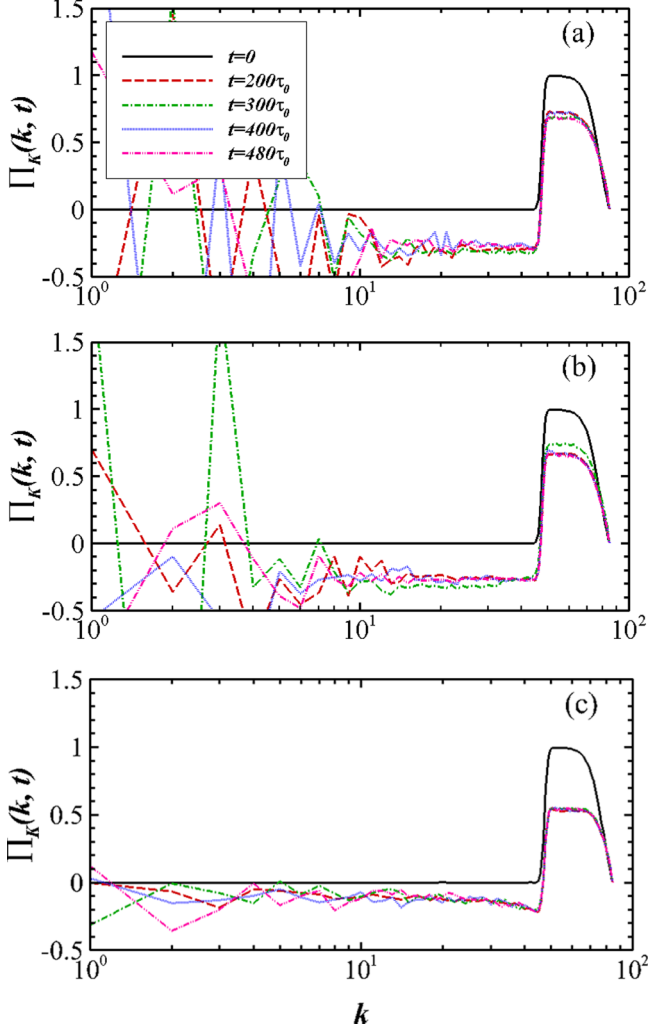


FIG. 9. The time evolution of the kinetic energy flux for (a) Run1, (b) Run2, and (c) Run3 at different times.

kinetic fluxes are totally different from those in purely rotating turbulence. This can be further demonstrated by the kinetic energy transfer functions

$$T_K(k_h, k_z) = \sum_{S(k_h), I(k_z)} \text{Re}[\hat{\mathbf{u}}^* \cdot \widehat{\mathbf{u}} \times \widehat{\boldsymbol{\omega}}], \quad (38)$$

where  $S(k_h)$  denotes a circular shell of horizontal wave numbers with central radius  $k_h$  and  $I(k_z)$  is an interval of vertical wave numbers with midpoint  $k_z$ . Figure 13 plots these functions at different times for Run2 and Run3, normalized by their largest absolute values. The results for Run2 are almost identical to those for Run1 (not shown), which are consistent with [16]. Initially, the kinetic energy transfer concentrates on the forcing scale  $k_f$ . After the addition of rotation and stratification, the intense transfer area is quickly carried to the  $k_z = 0$  plane and then moves towards smaller  $k_h$  with time [Figs. 13(a) and 13(b)]. For Run3, the kinetic energy is quickly transferred to the  $k_z = 0$  plane with small  $k_h$ , and compared with Run2, more areas where  $k_z \neq 0$  have nonzero  $T_K(k_h, k_z)$  [Figs. 13(c) and 13(d)].

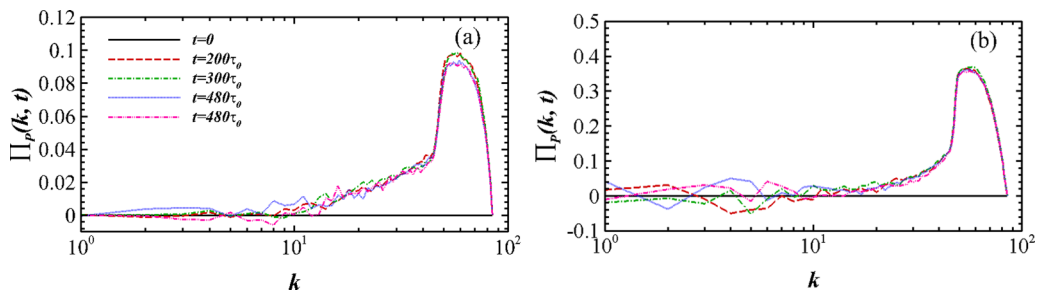


FIG. 10. The time evolution of the potential energy flux for (a) Run2 and (b) Run3 at different times.

To present how kinetic-potential energy exchange occurs among different horizontal and vertical wave numbers, we calculate the kinetic to potential energy transfer functions,

$$T_{KP}(k_h, k_z) = \sum_{S(k_h), I(k_z)} \text{Re}[N\hat{u}_z^* \hat{\phi}]. \quad (39)$$

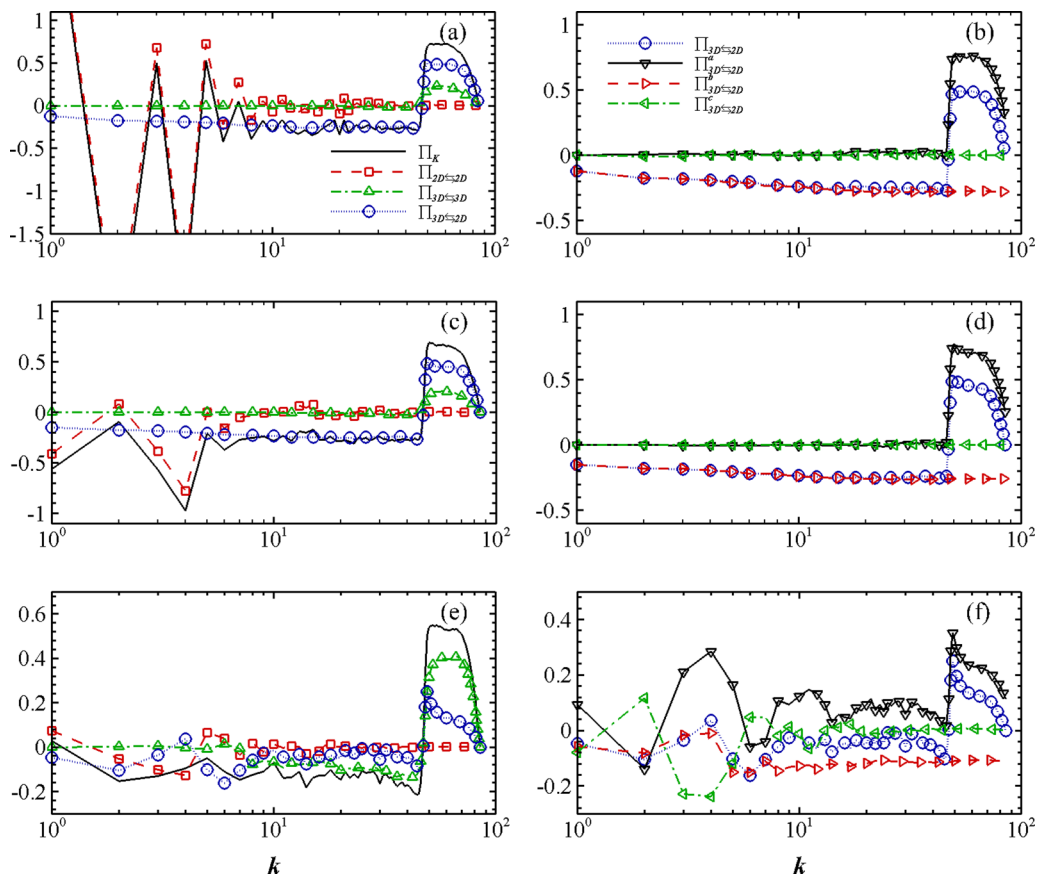


FIG. 11. (a), (c), (e) Total kinetic energy flux  $\Pi_K(k)$  and fluxes decomposed on the different 2D-3D interactions  $\Pi_{2D \rightleftharpoons 2D}(k)$ ,  $\Pi_{3D \rightleftharpoons 3D}(k)$  and  $\Pi_{3D \rightleftharpoons 2D}(k)$  [Eqs. (13)–(15)] and (b), (d), (f)  $\Pi_{3D \rightleftharpoons 2D}(k)$  and its three contributions of different classes of triads [Eqs. (16)–(18)] for (a), (b) Run1, (c), (d) Run2, and (e), (f) Run3. All the results come from one realization at time  $t = 480\tau_0$ .

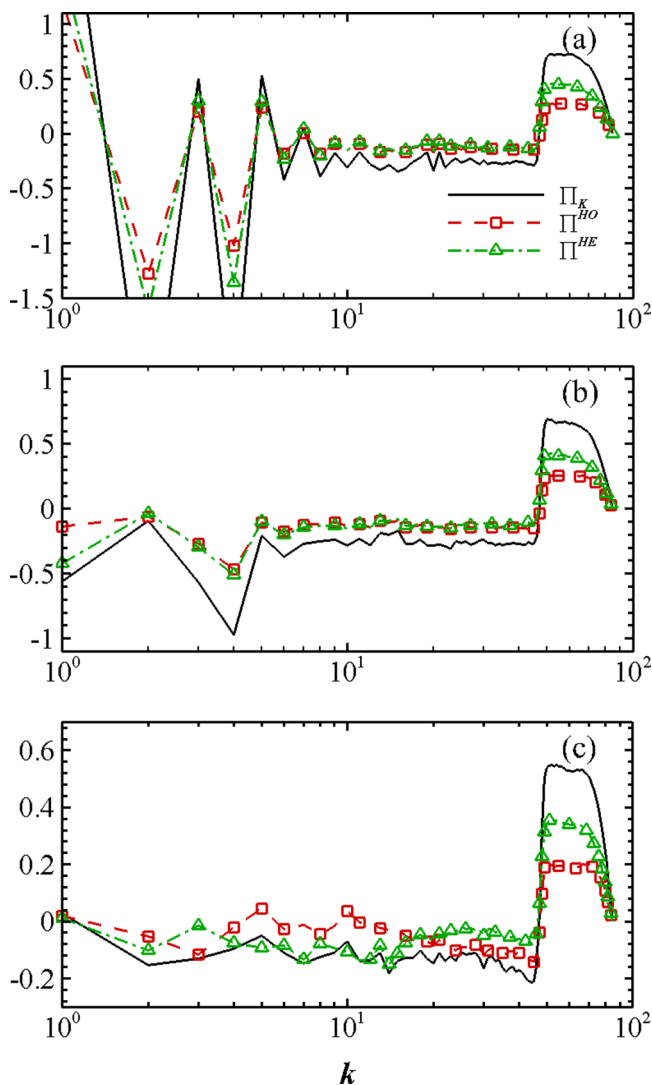


FIG. 12. Total kinetic energy flux  $\Pi_K(k)$ , homochiral energy flux  $\Pi^{HO}(k)$ , and heterochiral energy flux  $\Pi^{HE}(k)$  for (a) Run1, (b) Run2, and (c) Run3 from one realization at time  $t = 480\tau_0$ .

For Run2, Fig. 14 plots these kinetic to potential energy transfer functions at different times, normalized by their largest absolute values. Before rotation and stratification are added, there is no kinetic-potential energy exchange because  $\phi(x) = 0$ . At early times, the energy transfer occurs at almost all wave numbers near the  $k_z = 0$  plane [Figs. 14(a) and 14(b)]. The most intense modes then tend to have smaller  $k_h$  in the  $k_z = 0$  plane and at later times their  $k_h$  are fixed around  $5 \sim 10$  [Figs. 14(c) and 14(d)]. This is consistent with the above conclusion that the oscillation of the conversion rate of kinetic energy to potential energy is due to interactions of 2D inertia-gravity waves with  $k_h \approx 10$ . We note that the peak of  $T_{KP}$  with  $k_h$  around  $5 \sim 10$  might be caused by the 2D large-scale cyclone in the system, which is associated with an intense large-scale kinetic-potential energy exchange [27].



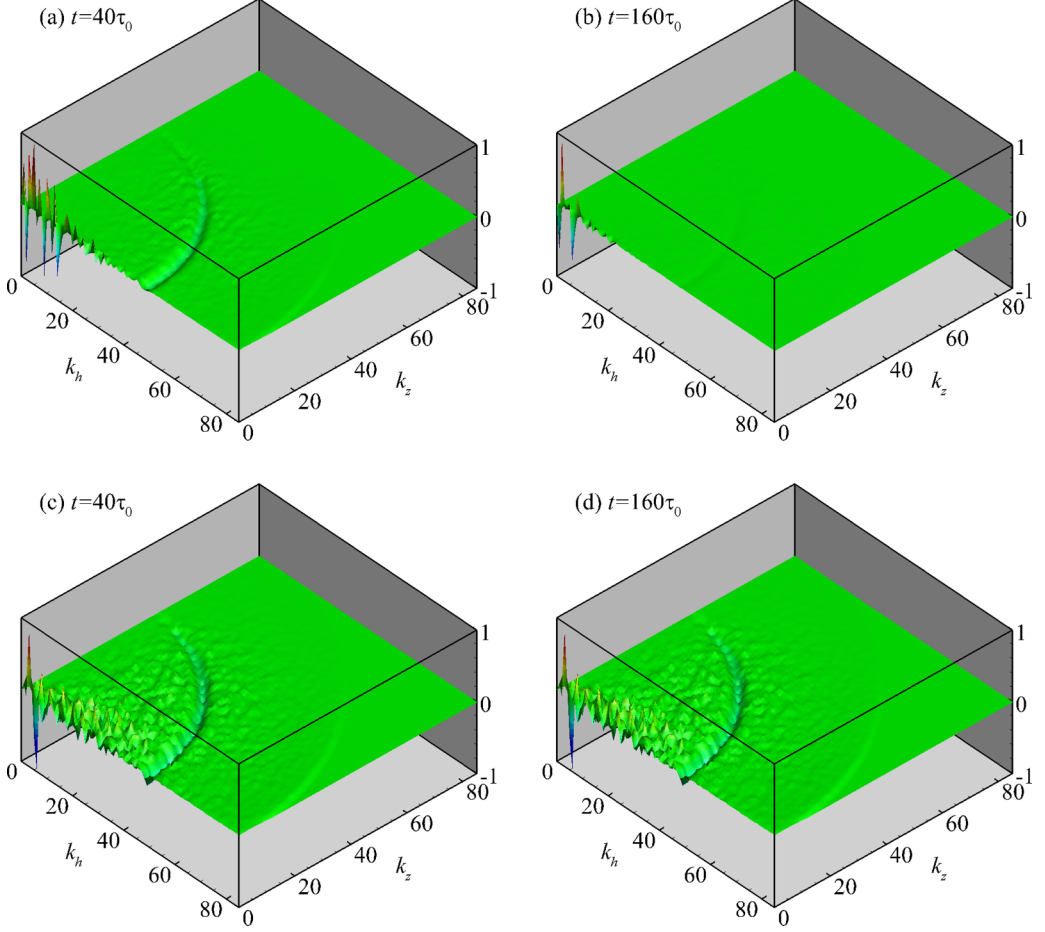


FIG. 13. Normalized kinetic energy transfer functions  $T_K(k_h, k_z)/|T_K|_{\max}$  at different times for (a), (b) Run2 and (c), (d) Run3.

#### D. Locality of kinetic energy cascade

To investigate the locality of kinetic energy flux, we adopt a filtering approach [46–48] which can resolve turbulent fields both in space and in scale. A “coarse-grained” field, which only contains large-scale ( $>l$ ) information, is defined by using a smooth low-pass filter,

$$\bar{u}_l(\mathbf{x}) = \int d\mathbf{r} G_l(\mathbf{r}) \mathbf{u}(\mathbf{x} + \mathbf{r}), \quad (40)$$

where  $G_l(\mathbf{r}) = l^{-3} G(\mathbf{r}/l)$  is a filtering kernel and  $G$  is chosen to be a Gaussian function  $G(\mathbf{r}) = (6/\pi)^{3/2} \exp(-6r^2)$  in our study. In this framework, the large-scale kinetic energy density  $e_l^k = 1/2|\bar{\mathbf{u}}_l|^2$  satisfies

$$\partial_t e_l^k + \nabla \cdot \mathbf{q}_l^k = -\Pi_l^k - \Phi_l - T_l + P_l^k - D_l^k, \quad (41)$$

where  $\mathbf{q}_l^k \equiv (e_l^k + \bar{p}_l) \bar{\mathbf{u}}_l$  represents the spatial transport of large-scale kinetic energy.  $\Pi_l^k = -\bar{\mathbf{S}}_l(\mathbf{x}, t) : \boldsymbol{\tau}_l(\mathbf{x}, t)$  is the local kinetic energy flux across scale  $l$ , where “:” is a double dot product,  $\bar{\mathbf{S}}_l = 1/2[(\nabla \bar{\mathbf{u}}_l) + (\nabla \bar{\mathbf{u}}_l)^T]$  is the large-scale strain tensor and  $\boldsymbol{\tau}_l = \overline{(\mathbf{u}\mathbf{u})}_l - \bar{\mathbf{u}}_l \bar{\mathbf{u}}_l$  is the subscale Reynolds stress tensor coming from the small-scale ( $<l$ ) velocity field which has been filtered

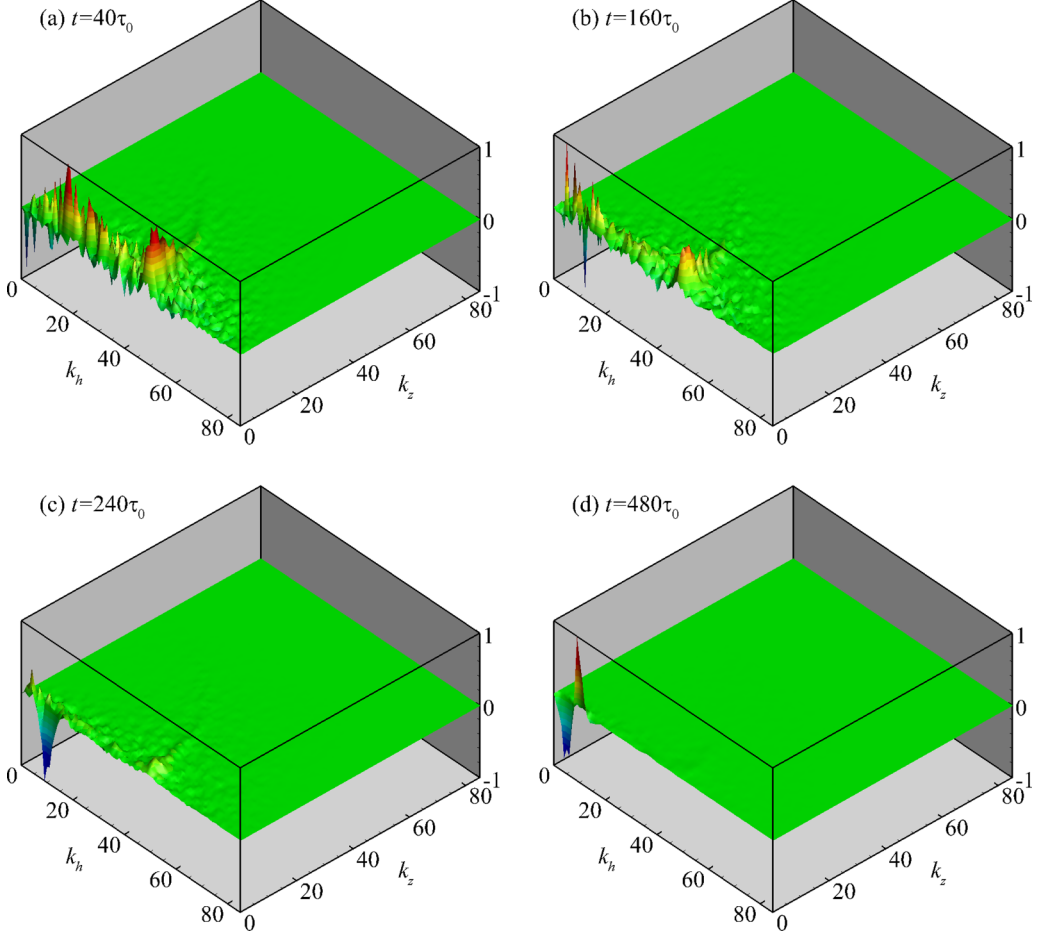


FIG. 14. Normalized kinetic to potential energy transfer functions  $T_{KP}(k_h, k_z)/|T_{KP}|_{\max}$  at different times for Run2.

out. The local kinetic energy flux induced by the rotation  $\Phi_l = f(\hat{\boldsymbol{\eta}} \times \bar{\mathbf{u}}_l) \cdot \bar{\mathbf{u}}_l = 0$  is trivial.  $T_l = N\bar{\phi}_l(\mathbf{e}_z \cdot \bar{\mathbf{u}}_l)$  represents the exchange of large-scale kinetic energy and potential energy.  $P_l^k = \bar{\mathbf{f}}_l \cdot \bar{\mathbf{u}}_l$  is the production term of large-scale kinetic energy and  $D_l^k$  is the dissipation term. Note that  $T_l$ ,  $P_l^k$  and  $D_l^k$  only involve large-scale ( $>l$ ) information. Therefore, they are insensitive to small-scale ( $<l$ ) flow fields and irrelevant with the energy transfer across scale  $l$ . In contrast,  $\Pi_l^k$  depends on fluctuations at small scales lesser than  $l$  and therefore contributes to the energy transfer across scales.

Eyink [49] presented a complete theoretical analysis about the scale locality. There is infrared (or ultraviolet) locality, if the contribution coming from the scale  $\Delta \gg l$  (or  $\delta \ll l$ ) to the energy flux across the scale  $l$  is negligible. To acquire a quantitative description of the locality, the stress is decomposed as in previous studies of two-dimensional turbulence [37,50] and magnetohydrodynamic turbulence [39]. Two discrete sequences of lengths  $\Delta^{(n)} = \lambda^n l$  and  $\delta^{(n)} = \lambda^{-n} l$  are introduced for  $\lambda = 1.25$  and  $n = 0, 1, 2, \dots$ . The stress from scales  $> \Delta^{(0)} = l$  can be decomposed as

$$\boldsymbol{\tau}_l = \sum_{n=0}^{\infty} \boldsymbol{\tau}_l^{\Delta^{(n)}}, \quad (42)$$

where  $\boldsymbol{\tau}_l^{\Delta^{(n)}} = \boldsymbol{\tau}_l(\bar{\mathbf{u}}_{\Delta^{(n)}}, \bar{\mathbf{u}}_{\Delta^{(n)}}) - \boldsymbol{\tau}_l(\bar{\mathbf{u}}_{\Delta^{(n+1)}}, \bar{\mathbf{u}}_{\Delta^{(n+1)}})$  is calculated as the stress due to  $\bar{\mathbf{u}}_{\Delta^{(n)}}$  minus the stress due to  $\bar{\mathbf{u}}_{\Delta^{(n+1)}}$ . Therefore,  $\Pi_l^{k,\Delta^{(n)}} = -\bar{\mathcal{S}}_l : \boldsymbol{\tau}_l^{\Delta^{(n)}}$  represents the contribution to kinetic energy flux from scales  $[\Delta^{(n)}, \Delta^{(n+1)})$ . There are two ways to decompose the stress from scales  $< \delta^{(0)} = l$  as follows:

$$\boldsymbol{\tau}_l = \sum_{n=0}^{\infty} \boldsymbol{\tau}_{l,1}^{\delta^{(n)}} = \sum_{n=0}^{\infty} \boldsymbol{\tau}_{l,2}^{\delta^{(n)}}, \quad (43)$$

where  $\boldsymbol{\tau}_{l,1}^{\delta^{(n)}} = \boldsymbol{\tau}_l(\bar{\mathbf{u}}_{\delta^{(n+1)}}, \bar{\mathbf{u}}_{\delta^{(n+1)}}) - \boldsymbol{\tau}_l(\bar{\mathbf{u}}_{\delta^{(n)}}, \bar{\mathbf{u}}_{\delta^{(n)}})$ ,  $\boldsymbol{\tau}_{l,2}^{\delta^{(n)}} = \boldsymbol{\tau}_l(\mathbf{u}'_{\delta^{(n)}}, \mathbf{u}'_{\delta^{(n)}}) - \boldsymbol{\tau}_l(\mathbf{u}'_{\delta^{(n+1)}}, \mathbf{u}'_{\delta^{(n+1)}})$ , and  $\mathbf{u}' = \mathbf{u} - \bar{\mathbf{u}}_l$  is the high-pass filtered field. Both decompositions have been adopted in previous studies [37,39,50] and their corresponding contributions to kinetic energy flux are  $\Pi_{l,1}^{k,\delta^{(n)}} = -\bar{\mathcal{S}}_l : \boldsymbol{\tau}_{l,1}^{\delta^{(n)}}$  and  $\Pi_{l,2}^{k,\delta^{(n)}} = -\bar{\mathcal{S}}_l : \boldsymbol{\tau}_{l,2}^{\delta^{(n)}}$ , respectively.  $\Pi_{l,1}^{k,\delta^{(n)}}$  and  $\Pi_{l,2}^{k,\delta^{(n)}}$  represent contributions from scales  $[\delta^{(n+1)}, \delta^{(n)})$  but from different subsets of triads. Given that  $l$  is an edge of the triads,  $\Pi_{l,1}^{k,\delta^{(n)}}$  quantifies the contribution from triads with one edge in  $[\delta^{(n+1)}, \delta^{(n)})$  and another edge smaller than  $\delta^{(n)}$ , while  $\Pi_{l,2}^{k,\delta^{(n)}}$  quantifies the contribution from triads with one edge in  $[\delta^{(n+1)}, \delta^{(n)})$  and another edge larger than  $\delta^{(n+1)}$ .

Using a filter length  $l = \pi/15$  in the inertial range, we calculated the contribution fractions to the kinetic energy flux across scale  $l$  from different scale intervals  $\langle \Pi_l^{k,\Delta^{(n)}} \rangle / \langle \Pi_l^k \rangle$ ,  $\langle \Pi_{l,1}^{k,\delta^{(n)}} \rangle / \langle \Pi_l^k \rangle$  and  $\langle \Pi_{l,2}^{k,\delta^{(n)}} \rangle / \langle \Pi_l^k \rangle$ . Their distributions are nearly unchanged when  $t \geq 320\tau_0$  and Fig. 15 shows the averaged contribution fractions. For all present simulations  $\langle \Pi_l^{k,\Delta^{(n)}} \rangle / \langle \Pi_l^k \rangle$  is vanishingly small [Fig. 15(a)], indicating that there is negligible contribution from large scales to the kinetic energy flux in the inertial range, thus there exists infrared locality of the kinetic energy cascade. Figure 15(b) shows that the smallest scales (largest  $n$ ) make the most significant  $\langle \Pi_{l,1}^{k,\delta^{(n)}} \rangle / \langle \Pi_l^k \rangle$ . Bands  $n = 4 \sim 6$  corresponding scales  $2.4l \sim 3.8l$  generate most of the kinetic flux. In contrast,  $\langle \Pi_{l,2}^{k,\delta^{(n)}} \rangle / \langle \Pi_l^k \rangle$  shows weak ultraviolet locality of the kinetic energy cascade in Fig. 15(c). Most of the kinetic flux results from bands  $n = 2 \sim 4$ , i.e., scales  $1.6l \sim 2.4l$ . Differences between Figs. 15(b) and 15(c) emerge from the different subsets of triads considered and this indicates that different scale decompositions of fluxes can suggest different results of the locality. In summary, the kinetic energy cascade is ultraviolet nonlocal. Figures 15(b) and 15(c) also show that  $\langle \Pi_{l,1}^{k,\delta^{(n)}} \rangle / \langle \Pi_l^k \rangle$  and  $\langle \Pi_{l,2}^{k,\delta^{(n)}} \rangle / \langle \Pi_l^k \rangle$  change negligibly with strengths of stratification, thus stratification does not change the locality of kinetic energy cascade in rotating stratified turbulence.

## V. SUMMARY

We investigated simulations of forced homogeneous rotating stratified turbulence for long integration times, focusing on the energy transfers across scales and kinetic-potential energy exchange in the inverse energy cascade range. Three simulations with intermediate forcing scales have been conducted with the same angular rotation rate and different stratification. Fourier space fluxes based on the 2D-3D decomposition and the helical decomposition have been measured to quantify the effects of stratification.

In rotating turbulence under weak stratification, we found that the distributions of different decomposed kinetic fluxes are similar to those in the purely rotating turbulence. The second contribution of 2D-3D coupling flux, coming from the 2D-kinetic-energy evolution equation, holds almost all the negative kinetic energy flux in the inertial range. At very small wave numbers, 2D interactions become important, which produce large negative fluxes among 2D modes. Homo- and heterochiral energy fluxes are equal in the backward transfer range. Compared with the purely rotating case, the weak stratification only weakens the magnitude of the inverse energy fluxes through the 3D kinetic-potential energy exchange. For rotating turbulence with strong stratification, the distributions of different decomposed kinetic fluxes are totally different from those in the purely

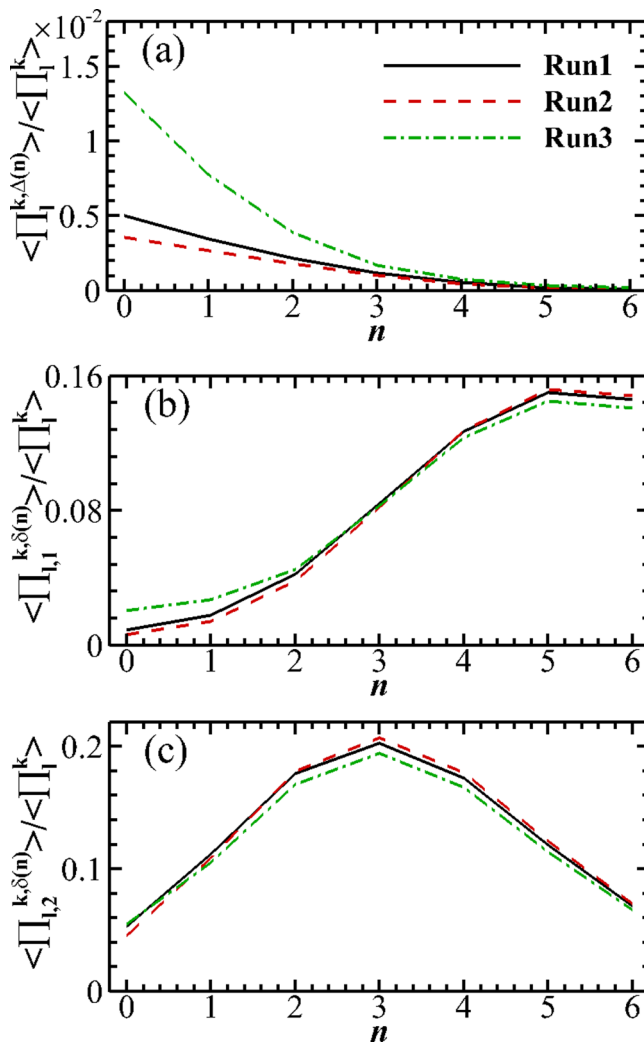


FIG. 15. Contribution fractions to the kinetic energy flux across scale  $l = \pi/15$ : (a) from scales  $[\Delta^{(n)}, \Delta^{(n+1)}]$ ; (b), (c) from scales  $[\delta^{(n+1)}, \delta^{(n)}]$  based on different decomposition methods.

rotating case. The negative values of 2D-3D coupling energy flux are small and the energy flux among 3D modes becomes significant near the forcing scales. Besides, the large-scale dynamics is dominated by kinetic energy fluxes from 2D interactions and 2D-3D coupling interactions. Moreover, homo- and heterochiral energy fluxes are not equal at different scales.

A systematic analysis of the kinetic-potential energy exchange has been conducted using the 2D-3D decomposition and the linear-eigenmode decomposition. Under weak stratification, 3D wave-vortical interactions induce a small constant conversion of kinetic energy to potential energy, and this conversion weakens the inverse cascade of kinetic energy. At later times, there is an oscillation of the total kinetic-potential energy exchange, which is produced by interactions between 2D inertia-gravity waves with fixed wave numbers. When the stratification is strong, the kinetic-potential energy exchange mainly exists in 3D modes and is dominated by wave-vortical interactions.

Finally, the locality of kinetic energy flux was investigated. The kinetic energy cascade is infrared local, while results of the ultraviolet locality depend on decompositions of the flux, which consider contributions from same scales but from different subsets of triads. The first kind of decomposition shows that most of the contribution occurs at the smallest scales, while the second indicates that the kinetic energy cascade is weakly ultraviolet local. Considering both of the decompositions indicates that the kinetic energy cascade is ultraviolet nonlocal. It was also found that strengths of stratification does not change the locality of the kinetic energy cascade.

We note that the  $Ro$  and  $Fr$  used in our work do not directly apply to typical geophysical flows on earth.  $Ro$  for atmospheric and oceanic flows at synoptic scales is about 0.1 and atmospheric flows on the earth have  $Ro > Fr$ . Therefore, readers should be careful when applying our conclusions to real atmospheric or oceanic flows. Stationary-state simulations are performed with a large-scale damping, and their results are similar as present study, which indicates that our conclusions are independent of confinement effects (periodicity effects).

### ACKNOWLEDGMENTS

This work has been supported by NSFC Grants No. 91752201, No. 11672123, and NSFC Basic Science Center Program (Grant No. 11988102); Department of Science and Technology of Guangdong Province Grant No. 2019B21203001; Shenzhen Science and Technology Innovation Commission Grant No. KQTD20180411143441009; Key Special Project for Introduced Talents Team of Southern Marine Science and Engineering Guangdong Laboratory (Guangzhou) (Grant No. GML2019ZD0103). Numerical simulations have been supported by Center for Computational Science and Engineering of Southern University of Science and Technology. M.W. acknowledges the support from Centers for Mechanical Engineering Research and Education at MIT and SUSTech.

- 
- [1] C. Hall and S. L. Dixon, *Fluid Mechanics and Thermodynamics of Turbomachinery* (Butterworth-Heinemann, London, 2013).
  - [2] J. Pedlosky, *Geophysical Fluid Dynamics* (Springer Science & Business Media, Berlin, 2013).
  - [3] G. K. Vallis, *Atmospheric and Oceanic Fluid Dynamics* (Cambridge University Press, Cambridge, 2017).
  - [4] J. J. Riley and M.-P. Lelong, Fluid motions in the presence of strong stable stratification, *Annu. Rev. Fluid Mech.* **32**, 613 (2000).
  - [5] O. Métais, P. Bartello, E. Garnier, J. Riley, and M. Lesieur, Inverse cascade in stably stratified rotating turbulence, *Dynam. Atmos. Ocean* **23**, 193 (1996).
  - [6] C. Cambon, N. N. Mansour, and F. S. Godeferd, Energy transfer in rotating turbulence, *J. Fluid Mech.* **337**, 303 (1997).
  - [7] J. Proudman, On the motion of solids in a liquid possessing vorticity, *Proc. R. Soc. London, Ser. A* **92**, 408 (1916).
  - [8] G. I. Taylor, Motion of solids in fluids when the flow is not irrotational, *Proc. R. Soc. London, Ser. A* **93**, 99 (1917).
  - [9] A. Ibbetson and D. Tritton, Experiments on turbulence in a rotating fluid, *J. Fluid Mech.* **68**, 639 (1975).
  - [10] E. Hopfinger, F. Browand, and Y. Gagne, Turbulence and waves in a rotating tank, *J. Fluid Mech.* **125**, 505 (1982).
  - [11] C. Morize and F. Moisy, Energy decay of rotating turbulence with confinement effects, *Phys. Fluids* **18**, 065107 (2006).
  - [12] P. Staplehurst, P. Davidson, and S. Dalziel, Structure formation in homogeneous freely decaying rotating turbulence, *J. Fluid Mech.* **598**, 81 (2008).
  - [13] L. Van Bokhoven, H. Clercx, G. Van Heijst, and R. Trieling, Experiments on rapidly rotating turbulent flows, *Phys. Fluids* **21**, 096601 (2009).
  - [14] N. Machicoane, F. Moisy, and P.-P. Cortet, Two-dimensionalization of the flow driven by a slowly rotating impeller in a rapidly rotating fluid, *Phys. Rev. Fluids* **1**, 073701 (2016).

- [15] P. Yeung and Y. Zhou, Numerical study of rotating turbulence with external forcing, *Phys. Fluids* **10**, 2895 (1998).
- [16] Q. Chen, S. Chen, G. L. Eyink, and D. D. Holm, Resonant interactions in rotating homogeneous three-dimensional turbulence, *J. Fluid Mech.* **542**, 139 (2005).
- [17] P. D. Mininni, A. Alexakis, and A. Pouquet, Scale interactions and scaling laws in rotating flows at moderate Rossby numbers and large Reynolds numbers, *Phys. Fluids* **21**, 015108 (2009).
- [18] L. Biferale, F. Bonaccorso, I. M. Mazzitelli, M. A. van Hinsberg, A. S. Lanotte, S. Musacchio, P. Perlekar, and F. Toschi, Coherent Structures and Extreme Events in Rotating Multiphase Turbulent Flows, *Phys. Rev. X* **6**, 041036 (2016).
- [19] P. C. Valente and V. Dallas, Spectral imbalance in the inertial range dynamics of decaying rotating turbulence, *Phys. Rev. E* **95**, 023114 (2017).
- [20] H. P. Greenspan, The theory of rotating fluids, Cambridge University Press, 1968.
- [21] F. Waleffe, Inertial transfers in the helical decomposition, *Phys. Fluids A: Fluid Dyn.* **5**, 677 (1993).
- [22] M. Buziccotti, H. Aluie, L. Biferale, and M. Linkmann, Energy transfer in turbulence under rotation, *Phys. Rev. Fluids* **3**, 034802 (2018).
- [23] J. R. Herring and O. Métais, Numerical experiments in forced stably stratified turbulence, *J. Fluid Mech.* **202**, 97 (1989).
- [24] L. M. Smith and F. Waleffe, Generation of slow large scales in forced rotating stratified turbulence, *J. Fluid Mech.* **451**, 145 (2002).
- [25] R. Marino, P. D. Mininni, D. Rosenberg, and A. Pouquet, Inverse cascades in rotating stratified turbulence: Fast growth of large scales, *Europhys. Lett.* **102**, 44006 (2013).
- [26] D. Oks, P. D. Mininni, R. Marino, and A. Pouquet, Inverse cascades and resonant triads in rotating and stratified turbulence, *Phys. Fluids* **29**, 111109 (2017).
- [27] T. Li, M. Wan, J. Wang, and S. Chen, Flow structures and kinetic-potential exchange in forced rotating stratified turbulence, *Phys. Rev. Fluids* **5**, 014802 (2020).
- [28] C. Leith, Nonlinear normal mode initialization and quasigeostrophic theory, *J. Atmos. Sci.* **37**, 958 (1980).
- [29] P. Bartello, Geostrophic adjustment and inverse cascades in rotating stratified turbulence, *J. atom. Sci.* **52**, 4410 (1995).
- [30] C. Herbert, A. Pouquet, and R. Marino, Restricted equilibrium and the energy cascade in rotating and stratified flows, *J. Fluid Mech.* **758**, 374 (2014).
- [31] E. Deusebio, A. Vallgren, and E. Lindborg, The route to dissipation in strongly stratified and rotating flows, *J. Fluid Mech.* **720**, 66 (2013).
- [32] B. T. Nadiga, Nonlinear evolution of a baroclinic wave and imbalanced dissipation, *J. Fluid Mech.* **756**, 965 (2014).
- [33] H. A. Kafiabad and P. Bartello, Spontaneous imbalance in the non-hydrostatic Boussinesq equations, *J. Fluid Mech.* **847**, 614 (2018).
- [34] A. Kolmogorov, Local structure of turbulence in an incompressible fluid at very high reynolds numbers, *Dokl. Akad. Nauk. SSSR* **30**, 299 (1941).
- [35] J. A. Domaradzki and D. Carati, An analysis of the energy transfer and the locality of nonlinear interactions in turbulence, *Phys. Fluids* **19**, 085112 (2007).
- [36] G. L. Eyink and H. Aluie, Localness of energy cascade in hydrodynamic turbulence. I. Smooth coarse graining, *Phys. Fluids* **21**, 115107 (2009).
- [37] Z. Xiao, M. Wan, S. Chen, and G. Eyink, Physical mechanism of the inverse energy cascade of two-dimensional turbulence: A numerical investigation, *J. Fluid Mech.* **619**, 1 (2009).
- [38] H. Aluie and G. L. Eyink, Scale Locality of Magnetohydrodynamic Turbulence, *Phys. Rev. Lett.* **104**, 081101 (2010).
- [39] Y. Yang, Y. Shi, M. Wan, W. H. Matthaeus, and S. Chen, Energy cascade and its locality in compressible magnetohydrodynamic turbulence, *Phys. Rev. E* **93**, 061102(R) (2016).
- [40] L. Bourouiba, D. Straub, and M. Waite, Non-local energy transfers in rotating turbulence at intermediate rossby number, *J. Fluid Mech.* **690**, 129 (2012).

- [41] L. Biferale, S. Musacchio, and F. Toschi, Inverse Energy Cascade in Three-Dimensional Isotropic Turbulence, *Phys. Rev. Lett.* **108**, 164501 (2012).
- [42] L. Biferale, S. Musacchio, and F. Toschi, Split energy–helicity cascades in three-dimensional homogeneous and isotropic turbulence, *J. Fluid Mech.* **730**, 309 (2013).
- [43] L. Bourouiba, Model of a truncated fast rotating flow at infinite Reynolds number, *Phys. Fluids* **20**, 075112 (2008).
- [44] P. Constantin and A. Majda, The Beltrami spectrum for incompressible fluid flows, *Commun. Math. Phys.* **115**, 435 (1988).
- [45] F. Waleffe, The nature of triad interactions in homogeneous turbulence, *Phys. Fluids A: Fluid Dyn.* **4**, 350 (1992).
- [46] M. Germano, Turbulence: The filtering approach, *J. Fluid Mech.* **238**, 325 (1992).
- [47] G. L. Eyink, Local energy flux and the refined similarity hypothesis, *J. Stat. Phys.* **78**, 335 (1995).
- [48] C. Meneveau and J. Katz, Scale-invariance and turbulence models for Large-Eddy simulation, *Annu. Rev. Fluid Mech.* **32**, 1 (2000).
- [49] G. L. Eyink, Locality of turbulent cascades, *Physica D: Nonlin. Phenom.* **207**, 91 (2005).
- [50] S. Chen, R. E. Ecke, G. L. Eyink, M. Rivera, M. Wan, and Z. Xiao, Physical Mechanism of the Two-Dimensional Inverse Energy Cascade, *Phys. Rev. Lett.* **96**, 084502 (2006).